Journal of Solid State Chemistry 182 (2009) 339–347

Contents lists available at ScienceDirect

Journal of Solid State Chemistry

journal homepage: www.elsevier.com/locate/jssc

Facile sonochemical synthesis and photoluminescent properties of lanthanide orthophosphate nanoparticles

Cuicui Yu [a,b], Min Yu [a,b], Chunxia Li [a], Xiaoming Liu [a], Jun Yang [a], Piaoping Yang [a], Jun Lin [a,*]

[a] State Key Laboratory of Rare Earth Resource Utilization, Changchun Institute of Applied Chemistry, Chinese Academy of Sciences, Changchun 130022, PR China
[b] Department of Chemistry, Northeast Normal University, Changchun 130024, PR China

ARTICLE INFO

Article history:
Received 19 June 2008
Received in revised form
14 October 2008
Accepted 19 October 2008
Available online 5 November 2008

Keywords:
Lanthanide orthophosphate
Ultrasonic irradiation
Nanoparticles
Formation mechanism
Luminescence

ABSTRACT

Uniform lanthanide orthophosphate $LnPO_4$ (Ln = La, Ce, Pr, Nd, Sm, Eu, Gd, Tb, Dy, Ho) nanoparticles have been systematically synthesized via a facile, fast, efficient ultrasonic irradiation of inorganic salt aqueous solution under ambient conditions without any surfactant or template. X-ray diffraction (XRD), scanning electron microscopy (SEM), transmission electron microscopy (TEM), high-resolution transmission electron microscopy (HRTEM), selected area electron diffraction (SAED), photoluminescence (PL) spectra as well as kinetic decays were employed to characterize the samples. The SEM and the TEM images show that the hexagonal structured lanthanide orthophosphate $LnPO_4$ (Ln = La, Ce, Pr, Nd, Sm, Eu, Gd) products have nanorod bundles morphology, while the tetragonal $LnPO_4$ (Ln = Tb, Dy, Ho) samples prepared under the same experimental conditions are composed of nanoparticles. HRTEM micrographs and SAED results prove that these nanostructures are polycrystalline in nature. The possible formation mechanism for $LnPO_4$ (Ln = La–Gd) nanorod bundles is proposed. Eu^{3+}-doped $LaPO_4$ and Tb^{3+}-doped $CePO_4$ samples were also prepared by using the same synthetic process, which exhibit an orange–red (Eu^{3+}:$^5D_0$–$^7F_{1,\,2,\,3,\,4}$) and green (Tb^{3+}, $^5D_4$–$^7F_{3,\,4,\,5,\,6}$) emission, respectively.

© 2008 Elsevier Inc. All rights reserved.

1. Introduction

Nanostructures which have received a well-designed composition and crystal structure can exhibit many interesting novel size- and shape-dependent properties, as well as their unique applications [1–5]. The generation of such small structures is essential to the advance of many areas of modern science and technology, and a number of physical- and chemical-based synthetic methodologies have been developed [6–12]. The synthesis of nanoparticles with well-controlled shapes, sizes, and structures is both scientifically and technically important. So far, much effort has been devoted to the fabrication of nanomaterials with unique shapes, such as ZnO doughnuts [13], CuO flowers [14], NiS with urchin-like nanostructures [15], dendritic micro-pines of magnetic Fe_2O_3 [16], ZnO cup [17], etc. However, they often suffer from the requirements of high temperature, special conditions, tedious procedures, and catalysts or templates. Thus, further explorations of novel morphology of inorganic materials by convenient synthesis methods with low synthesis temperature, cost-effective and less-complicated features are still a big challenge.

Recently, there has been an increased interest and research for lanthanide compounds, including LnF_3, Ln_2O_3, $Ln(OH)_3$, and $LnPO_4$ [18,19]. Among the large number of lanthanide inorganic salts, lanthanide phosphates are widely used as luminescent or laser materials, heat-resistant materials, and hosts for radioactive nuclear waste [20–24]. So far various $LnPO_4$ nanostructures, including redispersible $LnPO_4$ nanoparticles and $LnPO_4$ nanowires/nanorods of some highly polymorphs, have been synthesized [21–26]. Lanthanide orthophosphates have several polymorphic forms. They appear in hexagonal, tetragonal, and monoclinic modifications. The hexagonal structure is the low-temperature phase, and it can transform into the monoclinic structure, while the tetragonal structure is stable after calcinations at 900 °C [27,28]. Very recently, much progress has been made to notably increase the luminescent properties of lanthanide compound nanostructures and lanthanide-doped nanoparticles [29], particularly the pioneering research by Haase and coworkers on the lanthanide-doped $LnPO_4$ ($LnPO_4$:Ln^{3+}) nanoparticles [20,30]. Furthermore, Ce^{3+} and Tb^{3+} coactivated bulk $LaPO_4$ is a highly efficient and commercially applied green ($^5D_4$–$^7F_5$ of Tb^{3+} at 543 nm) phosphor in fluorescent lamps [31,32]. Up to now, most lanthanide phosphate nanomaterials with various 1D structures, such as nanorods, nanowires and nanocables, are prepared by hydrothermal or modified hydrothermal methods such as the hydrothermal microemulsion method and polymer-assisted hydrothermal methods [25,26,33]. However, to monitor

* Corresponding author. Fax: +86 431 5698041.
E-mail address: jlin@ciac.jl.cn (J. Lin).

0022-4596/$ - see front matter © 2008 Elsevier Inc. All rights reserved.
doi:10.1016/j.jssc.2008.10.023

the reactions taking place under extreme conditions in an autoclave is practically difficult and inconvenient. Therefore, an easy, efficient and general method needs to be developed for fabricating large number of nanostructured $LnPO_4$ materials.

The sonochemical process, which is simple and operated under ambient conditions, has been proved to be an available technique to obtain novel materials and prepare nanomaterials with unique morphology and unusual properties. During the sonication process, propagation of pressure waves is intense enough to make the formation, growth and implosive collapse of bubbles in liquid medium [34]. These bubbles generate a localized hotspot, which has the extreme high temperatures (>5000 K), pressures (>20 MPa), and cooling rates (10^{10} K s^{-1}) during acoustic cavitation. As a result, the sonication provides an ideal atmosphere for the preparation of nanomaterials. The advantages of this method include a rapid reaction rate, the controllable reaction conditions, and the ability to form materials with uniform shapes, narrow size distributions, and high purities. Here in this paper, we report the preparation of lanthanide orthophosphate $LnPO_4$ (Ln = La, Ce, Pr, Nd, Sm, Eu, Gd, Tb, Dy, Ho) nanoparticles via a facile, fast, efficient ultrasonic irradiation of inorganic salt aqueous solution under ambient conditions without any surfactant or template. The structure, formation mechanism and photoluminescence (PL) properties ($LaPO_4$:Eu^{3+} and $CePO_4$:Tb^{3+}) for these nanostructures are investigated in detail.

2. Experimental

2.1. Synthesis

All chemicals were of analytical grade, including Ln_2O_3 (Ln = La, Nd, Sm, Eu, Gd, Dy, Ho, Er, Tm, Yb, Lu), Pr_6O_{11} and Tb_4O_7 (all 99.99%) as well as $Ce(NO_3)_3 \cdot 6H_2O$ were purchased from Science and Technology Parent Company of Changchun Institute of Applied Chemistry. H_3PO_4 (Beijing Chemical Reagent Company). $Ln(NO_3)_3$ precursors were prepared by dissolving the corresponding lanthanide oxides in a diluted nitric acid solution, and the water in the solutions was evaporated by heating. In a typical synthesis, 23 mL of an aqueous solution of $Ln(NO_3)_3$ (2.3 mmol) was added to a diluted H_3PO_4 (30 mL, 11.5 mmol) solution under ultrasonic irradiation for 1 h. The pH value of the mixture was kept at 1–2. Ultrasonic irradiation was accomplished with a high-intensity ultrasonic probe (JCS-206 Jining Co. China, Ti horn, 100 W) immersed directly in the reaction solution. At the end of the sonication, a temperature of about 343 K was reached under ambient air without cooling. The resulting $LnPO_4$ precipitates were then centrifuged, washed with deionized water and absolute ethanol several times, and then dried in a vacuum at 333 K for 12 h for further characterization. $LaPO_4$:Eu^{3+} and $CePO_4$:Tb^{3+} samples were prepared in the similar way as that for pure $LnPO_4$. The doping concentration of Eu^{3+} (or Tb^{3+}) is 5 mol% of Ln^{3+} in $LaPO_4$ (or $CePO_4$) host.

2.2. Characterization

The XRD pattern was performed on a Rigaku-Dmax 2500 diffractometer at a scanning rate of 12°/min in the 2θ range from 10° to 70°, with graphite monochromatized Cu$K\alpha$ radiation ($\lambda = 0.15405$ nm). SEM micrographs were obtained using a field emission scanning electron microscope (FE-SEM, XL30, Philips). The morphology, particle size and crystalline phases were studied with the transmission electron microscopy (TEM). The TEM, high-resolution transmission electron microscopy (HRTEM) and selected area electron diffraction (SAED) pictures were recorded on a JEOL 2010 transmission electron microscope, using an accelerating voltage of 200 kV. The samples for TEM were prepared by dispersing the diluted suspension of the sample powder onto a carbon coated copper grid and then the grid was put at room temperature for several days. The PL excitation and emission spectra were recorded with a Hitachi F-4500 spectrophotometer equipped with a 150 W Xenon lamp as the excitation source. The luminescence decay curves were obtained from a Lecroy Wave Runner 6100 Digital Oscilloscope (1 GHz) using a 250 nm lasers (pulse width = 4 ns, gate = 50 ns) as the excitation. All the measurements were performed at room temperature.

3. Results and discussion

3.1. Formation, structure and morphology

Under the identical synthetic conditions (ultrasonic irradiation for 1 h), two different types of crystal structure of the $LnPO_4$ products have been identified by XRD analyzes. The XRD patterns of as-obtained hexagonal $LnPO_4$ (Ln = La, Ce, Pr, Nd, Sm, Eu, Gd) and tetragonal $LnPO_4$ (Ln = Tb, Dy, Ho) samples are shown in Fig. 1(a) and (b), respectively. Fig. 1a shows that all the reflection patterns can be readily indexed to a pure hexagonal phase [space group $P6_222$ (180)] for $LnPO_4$ (Ln = La→Gd) samples. The diffraction peaks shown in Fig. 1b are characteristic of a pure tetragonal phase [space group: $I4_1/amd$ (141)] for $LnPO_4$ (Ln = Tb→Ho) samples (JCPDS 32-1292 for $TbPO_4$ as a reference). The cell parameters of all the as-formed lanthanides orthophosphates are listed in Table 1. It can be seen from Fig. 1 that no other impurities can be detected in the synthesized products. Moreover, careful observation reveals that a systematic shift to the smaller d values (or higher 2θ degrees) for the diffraction peaks

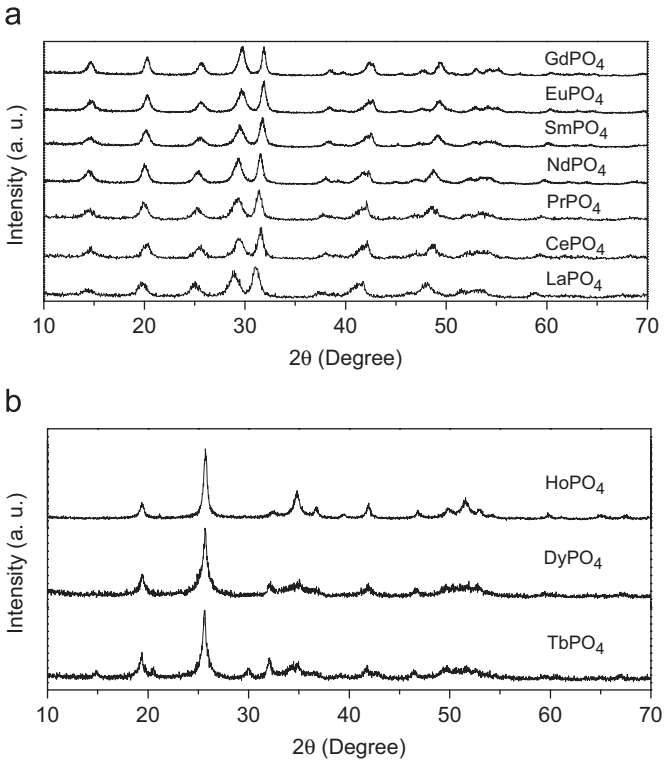

Fig. 1. XRD patterns of the as-prepared lanthanide phosphates (a) hexagonal (La→Gd)PO_4, (b) tetragonal (Tb→Ho)PO_4 nanoparticles.

Table 1
Refined lattice constants, the ionic radii of Ln^{3+}, and the average crystallite size (D) of $LnPO_4$ nanoparticles.

Samples (Ln^{3+})	Refined lattice constants		Ionic radii of Ln^{3+} (Å) CN = 8[a]	D from XRD (nm)
	a (Å)	c (Å)		
$LaPO_4$	7.046	6.468	1.160	12.0
$CePO_4$	7.045	6.421	1.143	14.2
$PrPO_4$	7.039	6.441	1.126	14.5
$NdPO_4$	7.031	6.409	1.109	11.3
$SmPO_4$	6.983	6.375	1.079	16.0
$EuPO_4$	6.942	6.352	1.066	16.6
$GdPO_4$	6.899	6.306	1.053	14.7
$TbPO_4$	6.946	6.075	1.040	17.5
$DyPO_4$	6.933	6.058	1.027	17.5
$HoPO_4$	6.922	6.048	1.015	19.6

[a] CN = Coordination number. Data adopted from Shannon, R.D. *Acta Cryst. A* 1976, 32, 751.

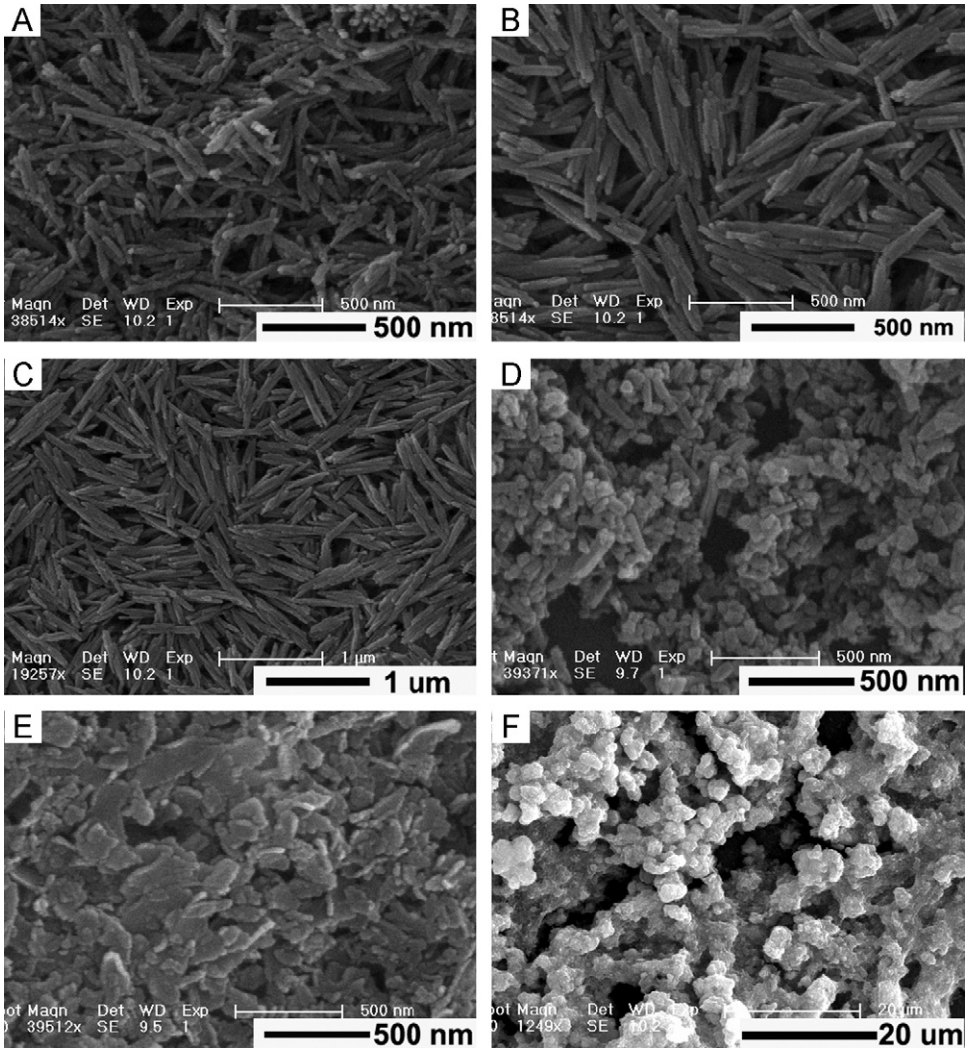

Fig. 2. SEM images with different magnifications of (A) $LaPO_4$, (B,C) $GdPO_4$ nanorod bundles and (D) $TbPO_4$, (E) $DyPO_4$, (F) $HoPO_4$ nanoparticles.

(Fig. 1a) and decrease of cell parameters (Table 1) from La to Gd due to the contraction of the ionic radii of lanthanides for the hexagonal type (La→Gd)PO_4. The nanocrystallite sizes of the samples of the hexagonal phase (La→Gd)PO_4 and the tetragonal phase (Tb→Ho)PO_4 can be roughly estimated from the Scherrer equation, $D = 0.941\lambda/\beta\cos\theta$, where D is the average grain size, λ is the X-ray wavelength (0.15405 nm), θ and β are the diffraction angle and full-width at half-maximum (FWHM) of an observed

peak, respectively [35]. The strongest peak (102) at $2\theta = 31.041^\circ$ of the hexagonal phase and (200) around 25.620° of the tetragonal phase were used to calculate the average crystallite size (D), respectively. The estimated average crystallite sizes are 12.0 nm for $LaPO_4$ and 17.5 nm for $TbPO_4$, respectively. The results for others are listed in Table 1.

The morphologies and microstructure of the as-prepared hexagonal and tetragonal $LnPO_4$ samples were investigated with SEM, TEM HRTEM, and SAED. Fig. 2 shows the typical SEM images of the as-formed $LaPO_4$ (A), $GdPO_4$ (B, C), $TbPO_4$ (D), $DyPO_4$ (E) and $HoPO_4$ (F) samples, respectively. The SEM images of the $LaPO_4$ (Fig. 2A) and $GdPO_4$ (Fig. 2B and C) samples demonstrate that they have nanorod bundles shape with the lengths of about 500 nm and diameter of about 100 nm. The careful observation of SEM image indicates that these 1D nanorod bundles are composed of individual parallel nanorods which self-organize into bundles shape assemblies (Fig. 2A–C). However, the $TbPO_4$, $DyPO_4$, $HoPO_4$ (Fig. 2D–F) shows the particle-like morphology. Representative TEM images of hexagonal (La→Gd)PO_4 nanorods and the tetragonal phase (Tb→Ho)PO_4 nanoparticles are depicted in Figs. 3A–J, respectively. It clearly reveals that the hexagonal (La→Gd)PO_4 products are primarily composed of nanorod bundles and almost no nanoparticles were observed, indicating high yield 1D nanostructures can be obtained by this method. So it is also implying that the nanorod bundles are self-assembled from the smaller nanorods. However, in Fig. 3H–J tetragonal type

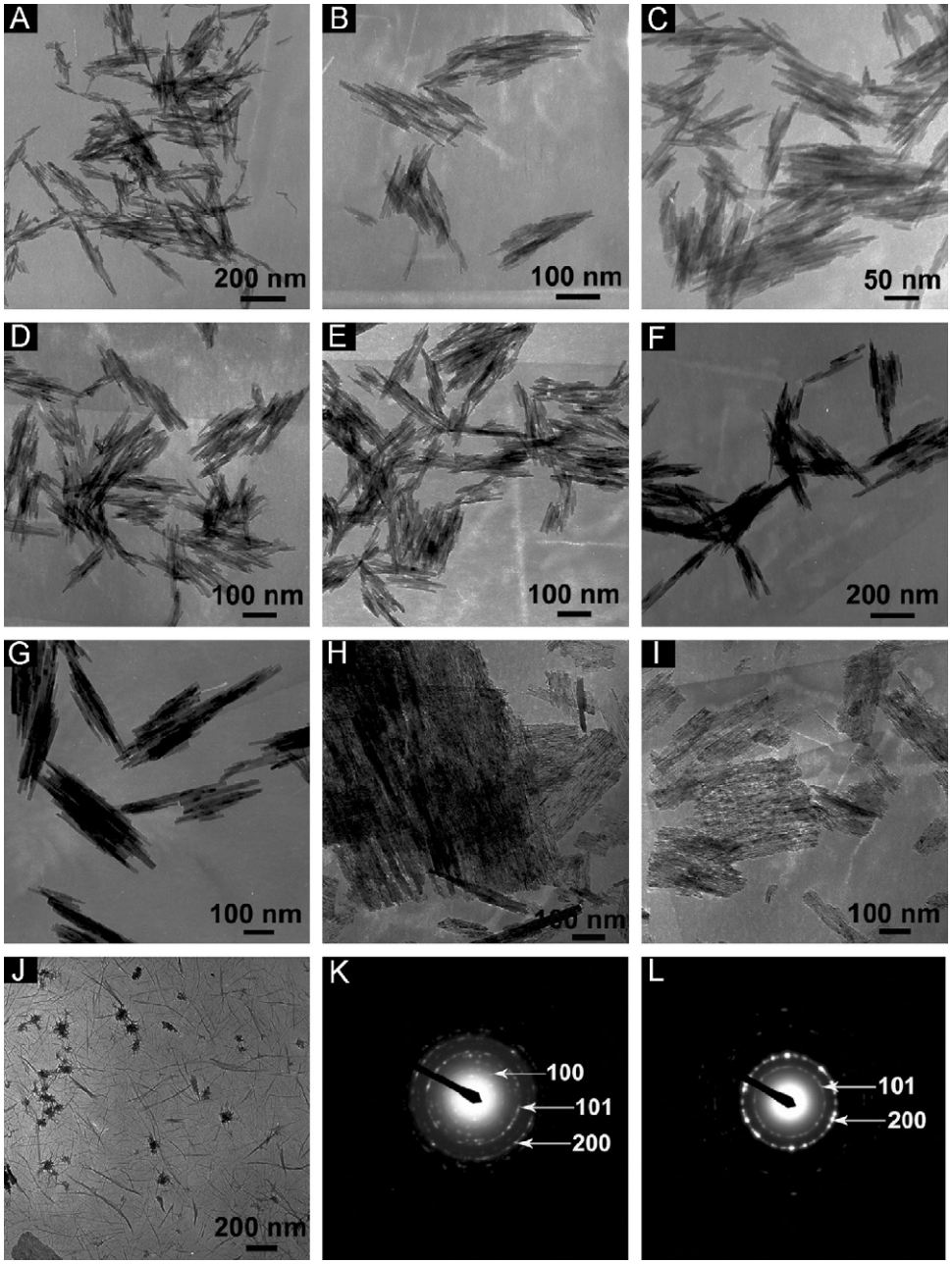

Fig. 3. Typical TEM images of the lanthanide phosphates samples (A) $LaPO_4$, (B) $CePO_4$, (C) $PrPO_4$, (D) $NdPO_4$, (E) $SmPO_4$, (F) $EuPO_4$, (G) $GdPO_4$, (H) $TbPO_4$, (I) $DyPO_4$, (J) $HoPO_4$ together with the SAED pattern of (K) $GdPO_4$ and (L) $DyPO_4$ nanoparticles.

(Tb→Ho)PO_4 have the particle-like morphology. The SAED pattern (Fig. 3(K, L) taken from hexagonal $GdPO_4$ and tetragonal $DyPO_4$ show a set of rings instead of spots, revealing that they are polycrystalline in nature. The similar results were also obtained for the other lanthanide orthophosphates. Fig. 4A–D show the HRTEM images hexagonal phase $GdPO_4$ nanorods and tetragonal phase $TbPO_4$, $DyPO_4$, $HoPO_4$ nanoparticles, respectively. From the HRTEM images, we can see the well-resolved lattice fringes clearly, and the distance (0.48 nm for $GdPO_4$, 0.38 nm for $TbPO_4$, 0.39 nm for $DyPO_4$ and $HoPO_4$) between the adjacent lattice fringes just corresponds to the interplanar distance of (101) planes for $GdPO_4$ and (200) planes for $TbPO_4$, $DyPO_4$ and $HoPO_4$, agreeing well with the d (101) and d (200) spacing of the literature values (0.435 nm in JCPDS No. 04-0644 for $GdPO_4$, 0.3475 nm in JCPDS

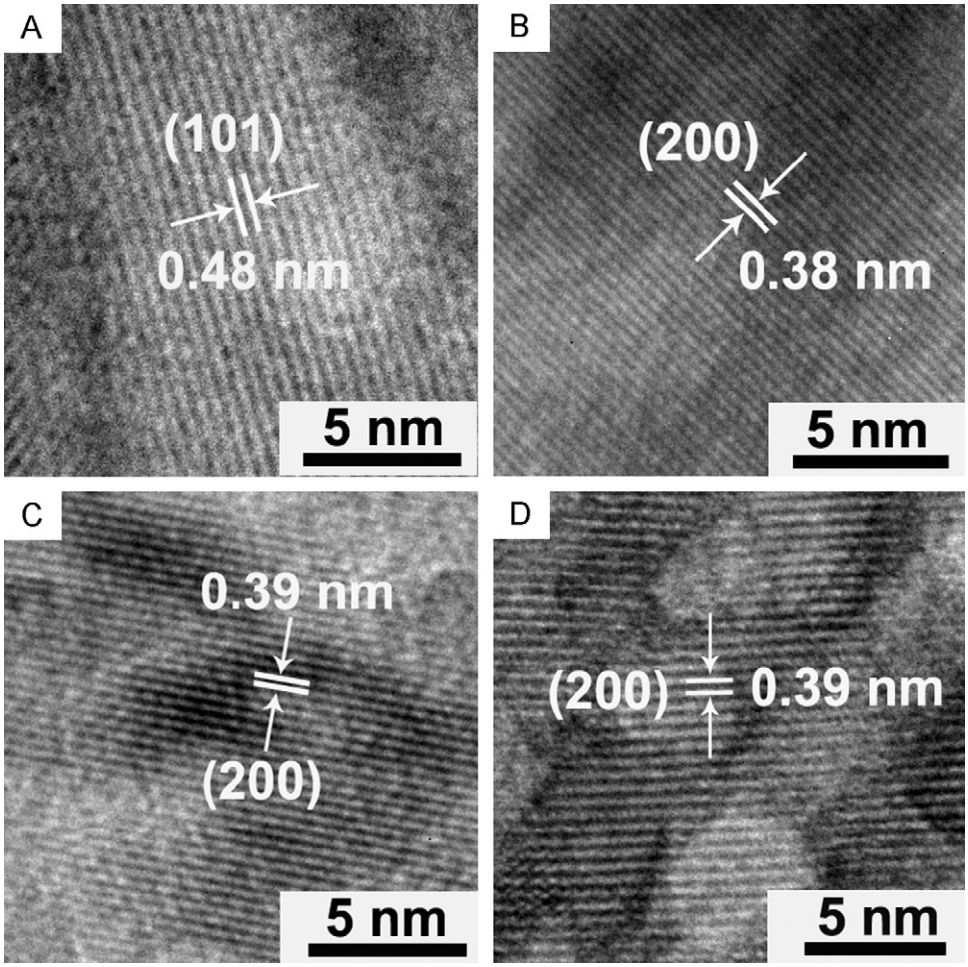

Fig. 4. HRTEM images of (A) $GdPO_4$, (B) $TbPO_4$, (C) $DyPO_4$ and (D) $HoPO_4$ nanoparticles.

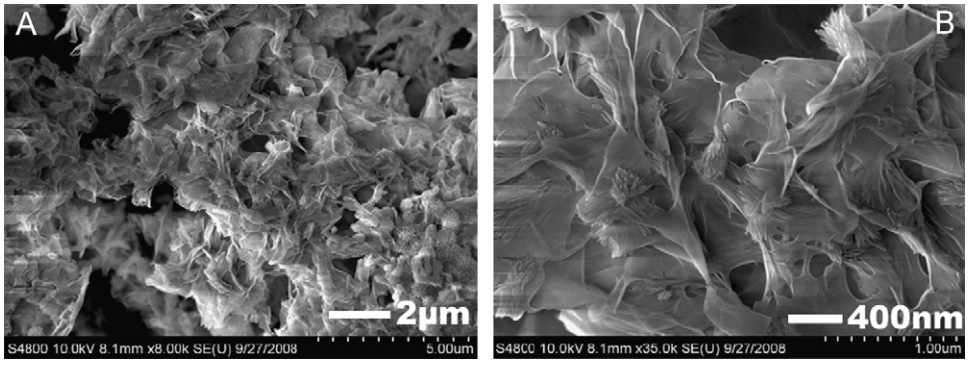

Fig. 5. SEM images of the $GdPO_4$ sample prepared through stirring for 1 h without ultrasonication at room temperature.

No. 32-1292 for $TbPO_4$, 0.346 nm in JCPDS No. 26-0593 for $DyPO_4$ and 0.345 nm in JCPDS No. 26-0746 for $HoPO_4$). The lattice fringes corresponding to the interplanar distance are also revealing that $GdPO_4$ is hexagonal phase and $TbPO_4$, $DyPO_4$, $HoPO_4$ are tetragonal phase.

3.2. The possible growth mechanism of hexagonal $(La \rightarrow Gd)PO_4$ nanorod bundles

It is believed that the growth of hexagonal $(La \rightarrow Gd)PO_4$ nanorod bundles are not template-directed or catalyst-assisted, because no additional surfactants or templates were introduced during the formation. At first, note that the ultrasonic irradiation plays an important role in the formation of $(La \rightarrow Gd)PO_4$ nanoparticles with nanorod bundles morphology in our current experimental conditions. In order to validate it, a contrastive experiment was conducted to fabricate $GdPO_4$ through stirring for 1 h without ultrasonication at room temperature. The shape of the corresponding product is irregular (Fig. 5A and B). In the results presented here, the instantaneous high-temperature and high-pressure field developed during ultrasonic irradiation helped to control the particle growth of $(La \rightarrow Gd)PO_4$ nanorod bundles, possibly because of the short collapse between a few nucleation centers in collapsing bubbles [36]. In addition, we take $GdPO_4$ as a representative example to conduct detailed time-dependent experiments under ultrasonic irradiation to investigate the formation mechanism of nanorod bundles. Fig. 6 shows the SEM images of the corresponding intermediates. At $t = 5$ min, the product is composed of a large amount of nanowires which interconnect to each other to form network-like structures. Furthermore, a small quantity of nanorod bundles can be clearly observed. However, more careful examination of SEM image indicates that these nanorod bundles are felted by nanowire network structure (Fig. 6A). With the reaction time up to 15 min, the dominant morphology of the products is complete nanorod bundles (Fig. 6B). However, the enlarged SEM image shows that these nanorod bundles are still felted by nanowires (insert in Fig. 6B). After 30 min of growth, the nearly more uniform and monodisperse nanorod bundles segregate from each other and nanowires completely disappear, as presented in Fig. 6C. From Fig. 6D, it can be clearly seen that these nanorod bundles consist of smaller parallel nanorods instead of nanowires presented in the early stage. On the other hand, the $LnPO_4$ $(La \rightarrow Gd)PO_4$ nanorods that have been fabricated here have a hexagonal crystal structure, similar to that of ZnO [37] and $Ln(OH)_3$ [38,39], which are known to exhibit anisotropic growth. In principle, the anisotropic growth of a crystal should be favorable for the formation of nanorods. Because of the hexagonal crystal structures observed here, which are characteristic of highly anisotropic growth, we believe that the habit of anisotropic growth is the inherent reason for the formation of $(La \rightarrow Gd)PO_4$ nanorod bundles.

3.3. Luminescent properties $LaPO_4$:0.05Eu^{3+}

The Eu^{3+}-doped $LaPO_4$ nanostructures exhibit a strong orange–red emission under the irradiation of short wavelength UV light. Fig. 7(a) and (b) shows the excitation and emission spectra for $LaPO_4$:0.05Eu^{3+}, respectively. The excitation spectrum (Fig. 7a) consists of a broad intense band with a maximum at 245 nm and some narrow excitation peaks at 320 ($^7F_0$–$^5H_6$), 366 ($^7F_0$–$^5D_4$), 397 ($^7F_0$–$^5L_6$), 418 ($^7F_0$–$^5D_3$), 467 nm ($^7F_0$–$^5D_2$) due to the general f–f transitions within the Eu^{3+} $4f^6$ electron configuration in the longer wavelength region (300–500 nm). The strong broad band at 245 nm is caused by the oxygen-to-europium charge transfer band (CTB). Upon excitation into the CTB of Eu^{3+} at 245 nm, the emission spectra are composed of $^5D_0$–^7F_J ($J = 1, 2, 3, 4$) emission

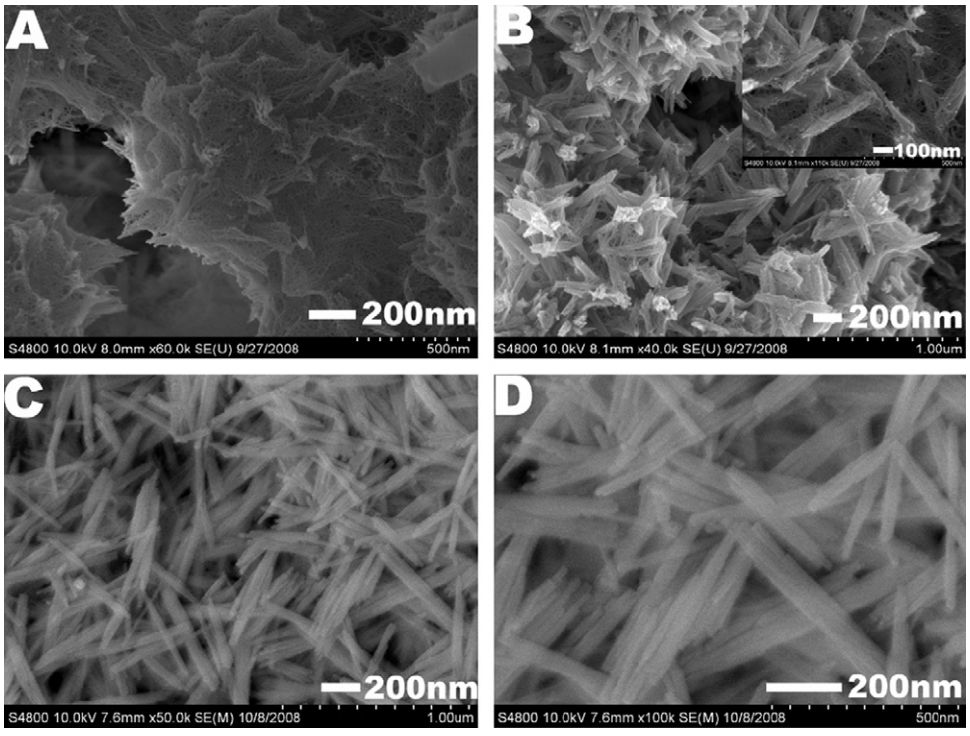

Fig. 6. SEM images showing morphology evolution for $GdPO_4$ products as a function of reaction time of (A) 5 min, (B) 15 min, and (C, D) 30 min under ultrasonic irradiation. Inset in part B: the corresponding higher-magnification SEM image.

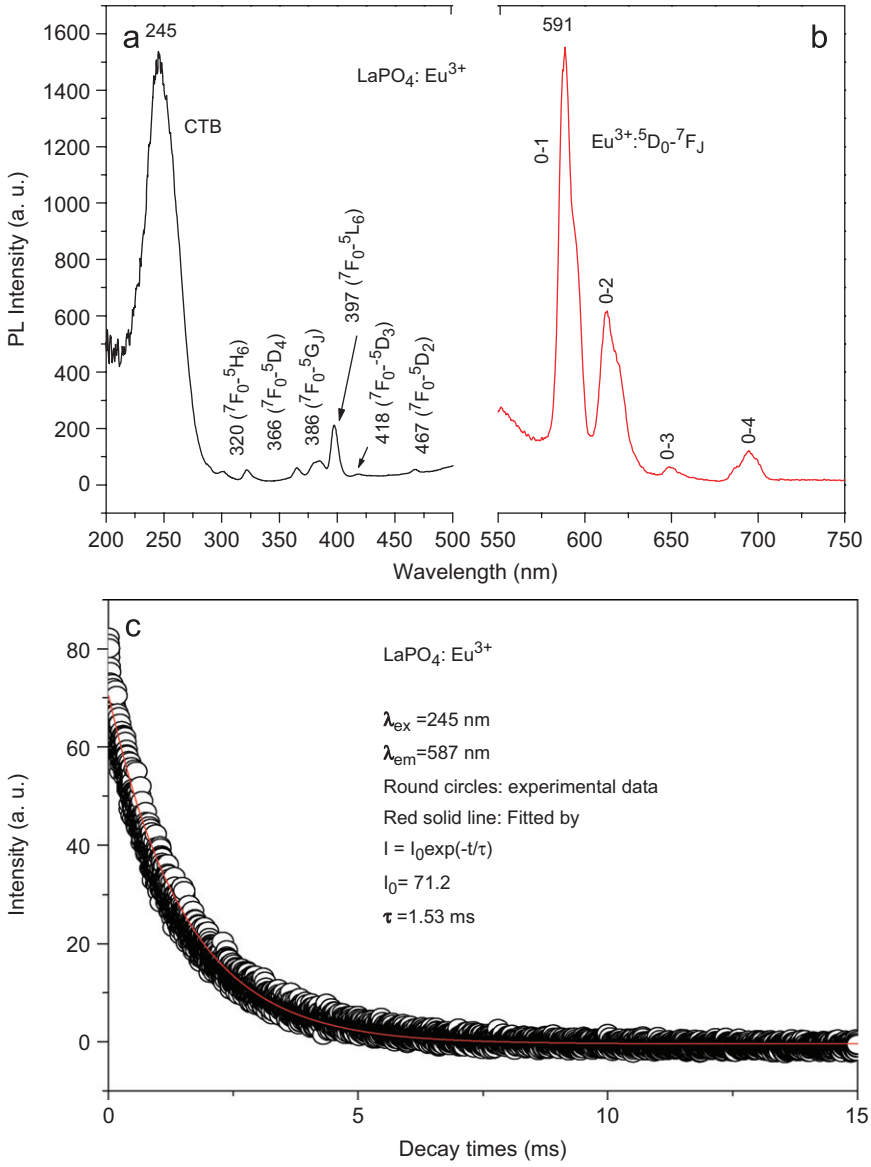

Fig. 7. The excitation (a), emission (b) spectra and decay curve (c) of the as-prepared $LaPO_4$:0.05Eu^{3+} nanorods.

lines of Eu^{3+}, with the magnetic-dipole transition $^5D_0$–$^7F_1$ (591 nm) being the most prominent group (Fig. 7b). This is characterized by orange–red emission. No emission from the higher energy levels ($^5D_1$, $^5D_2$) of Eu^{3+} is detected due to multiphoton relaxation based on the vibration of phosphate groups (1078 cm^{-1}), which is able to bridge the gaps between the higher energy levels ($^5D_1$, $^5D_2$) and the lowest $^5D_0$ level of Eu^{3+} effectively. These luminescent properties of Eu^{3+} in the (La→Gd)PO_4 1D nanostructures are basically in agreement with those previously reported [19,40,41]. The orange–red emissions for the nanorods can be further confirmed by the CIE (Commission Internationale de l'Eclairage 1931 chromaticity) coordinates for the emission spectra of $LaPO_4$:0.05Eu^{3+} ($x = 0.5074$, $y = 0.3495$), as shown in Fig. 8 (point a, orange–red region).

The luminescent decay curve of Eu^{3+} in $LaPO_4$:0.05Eu^{3+} nanorods are shown in Fig. 7c. In general, the curve can be well fitted into a single exponential function as $I = I_0 \exp(-t/\tau)$, in which τ is the decay lifetime [42]. The lifetime of Eu^{3+} ($^5D_0$ excited state) in $LaPO_4$ host lattices is determined to be 1.53 ms, which is in the same order of magnitude as that reported in Ref. [43].

3.4. *$CePO_4$ and $CePO_4$:0.05Tb^{3+}*

Fig. 9(a) and (b) shows the excitation and emission spectra of the $CePO_4$ sample. The excitation spectrum contains a strong band at 280 nm and two weak bands at 260 and 236 nm, which correspond to the transitions from the ground state $^2F_{5/2}$ of Ce^{3+} to the different components of the excited Ce^{3+} 5d states split by the crystal field (Fig. 9a). The emission spectrum exhibits a strong consist of a strong band peaking at 352 nm arise from the 5d–4f transition of Ce^{3+} (Fig. 9b) [44].

Under short UV excitation $CePO_4$:0.05Tb^{3+} nanorod sample shows a strong green emission. Fig. 9(c) and (d) shows the excitation and emission spectra of $CePO_4$:0.05Tb^{3+} nanorods. The excitation spectrum of $CePO_4$:0.05Tb^{3+} (Fig. 9c) consists mainly a

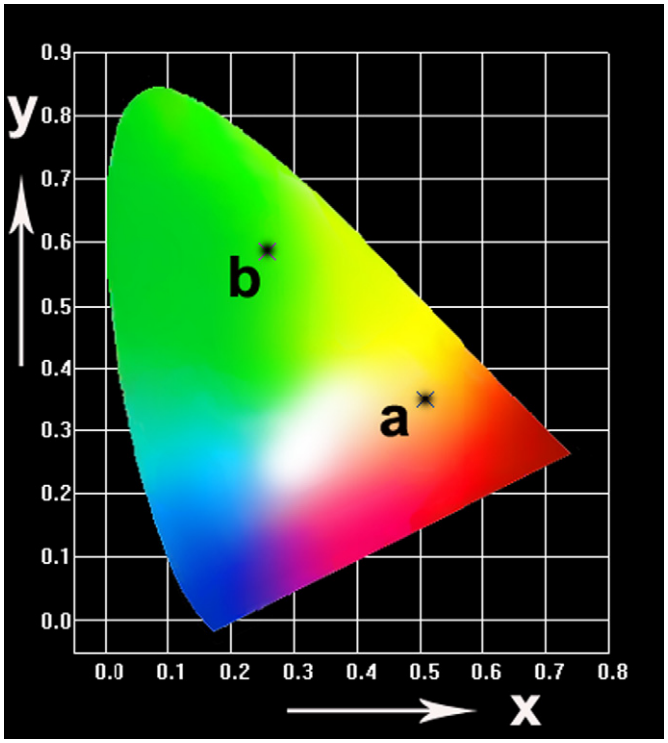

Fig. 8. The CIE chromaticity diagram for (a) $LaPO_4$:0.05Eu^{3+} and (b) $CePO_4$:0.05Tb^{3+} nanorods.

broad and strong band with a maximum at 280 nm due to the 4f–5d transition of Ce^{3+} (which is similar to that of $CePO_4$ in Fig. 9a), indicating an energy transfer from Ce^{3+} to Tb^{3+} in $CePO_4$:0.05Tb^{3+} sample [45]. Upon excitation into the Ce^{3+} at 280 nm, the obtained emission spectrum (Fig. 9d) consists mainly of five peaks at 352 (weak) from Ce^{3+} and 490 nm (weak, $^5D_4$–$^7F_6$), 543 nm (strong, $^5D_4$–$^7F_5$), 590 nm (weak, $^5D_4$–$^7F_4$) and 623 nm (weak, $^5D_4$–$^7F_3$) from Tb^{3+}, respectively [18,46]. This further indicates the energy transfer from Ce^{3+} to Tb^{3+} in $CePO_4$:0.05Tb^{3+} sample. The green emission for the $CePO_4$:0.05Tb^{3+} nanorods can be confirmed by the CIE coordinates for the emission spectra of $CePO_4$:0.05Tb^{3+} ($x = 0.2581$, $y = 0.5851$), as shown in Fig. 8 (point b, green region). The luminescent decay curve of Tb^{3+} ($^5D_4$–$^7F_5$ under excitation of Ce^{3+} at 280 nm) in $CePO_4$:0.05Tb^{3+} from single-exponential behavior, and the lifetime of Tb^{3+} is determined to be 1.97 ms, as shown in Fig. 9e [47,48].

4. Conclusions

Hexagonal $LnPO_4$ (Ln = La, Ce, Pr, Nd, Sm, Eu, Gd) and tetragonal $LnPO_4$ (Ln = Tb, Dy, Ho) nanoparticles have been successfully synthesized by a simple and facile sonochemical method. The hexagonal type (La→Gd)PO_4 nanoparticles are rod bundles-like with an equatorial diameter of 100 nm and up lengths of 500 nm, which are composed of smaller nanorods. However, the tetragonal type (Tb→Ho)PO_4 shows the particle-like morphology. A systematic study of photoluminescence in Eu^{3+} and Tb^{3+}-doped $LaPO_4$ and $CePO_4$ were carried out. Under the excitation of UV light, the hexagonal type $LaPO_4$:Eu^{3+} and $CePO_4$:Tb^{3+} nanorods exhibit orange–red (591) and green (547) luminescence, respectively. The strong green emission of Tb^{3+} in $CePO_4$:Tb^{3+} nanorods results from an efficient energy transfer from Ce^{3+} to Tb^{3+} and they may be a promising candidate for device applications. The synthesis of lanthanide orthophosphate nanomaterials by ultrasonication may open a broad frontier of uses, including in vivo applications.

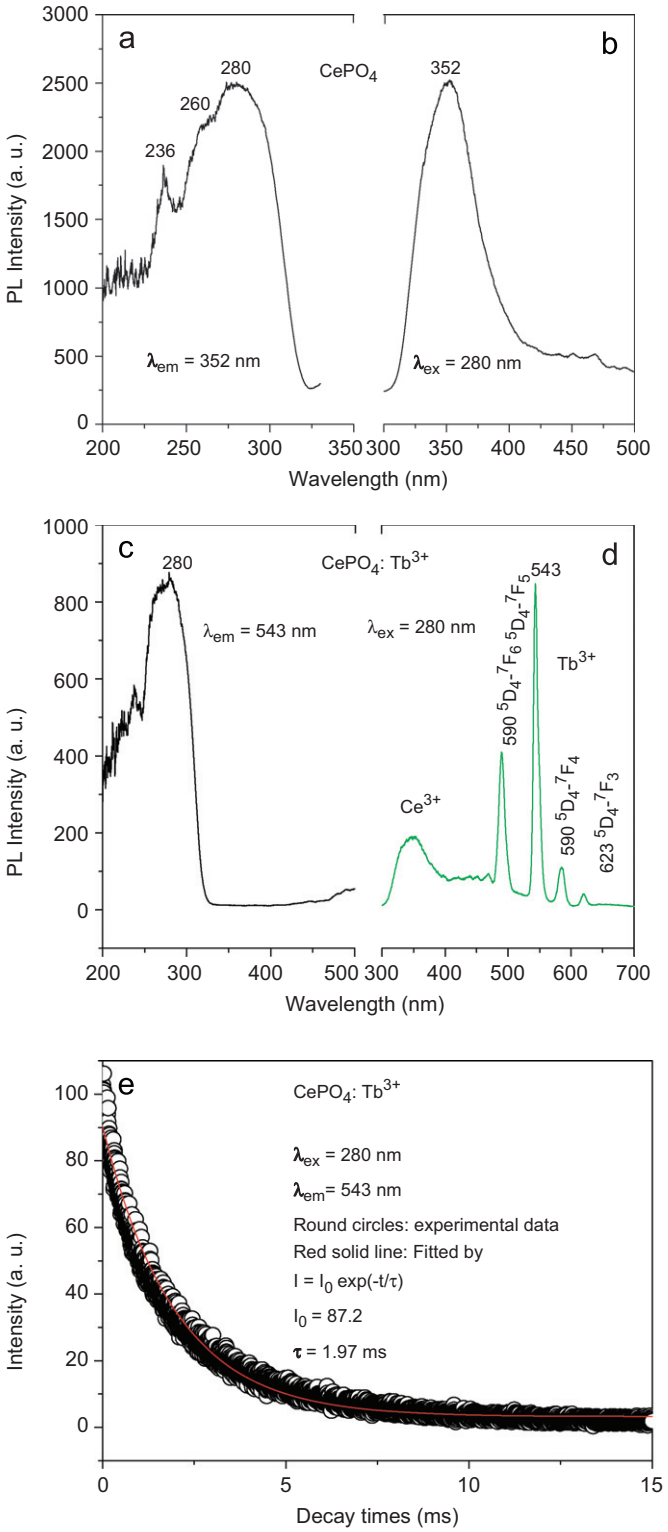

Fig. 9. The excitation and emission spectra of $CePO_4$ (a, b) and $CePO_4$:0.05Tb^{3+} (c, d) as well as the decay curve of Tb^{3+} in $CePO_4$:0.05Tb^{3+} (e).

Acknowledgments

This project is financially supported by the foundation of "Bairen Jihua" of Chinese Academy of Science, the MOST of China

(2007CB935502), the National Natural Science Foundation of China (50572103, 20431030, 00610227, 50872131).

References

[1] A.P. Alivisatos, Science 271 (1996) 933.
[2] C.B. Murray, C.R. Kagan, M.G. Bawendi, Annu. Rev. Mater. Sci. 30 (2000) 545.
[3] S.J. Park, T.A. Taton, C.A. Mirkin, Science 295 (2002) 1503.
[4] A.T. Bell, Science 299 (2003) 1688.
[5] M. Law, H. Kind, B. Messer, F. Kim, P.D. Yang, Angew. Chem. 114 (2002) 2511.
[6] Y. Wu, H. Yan, M. Huang, B. Messer, J.H. Song, P. Yang, Chem. Eur. J. 8 (2002) 1261.
[7] H. Zhu, C. Xu, D. Wu, B. Wei, R. Vajtai, P.M. Ajayan, Science 296 (2002) 884.
[8] Y.G. Sun, Y.N. Xia, Science 298 (2002) 2176.
[9] T.J. Hu, T.W. Odom, C.M. Lieber, Acc. Chem. Res. 32 (1999) 435.
[10] G.R. Patzke, F. Krumeich, R. Nesper, Angew. Chem. 114 (2002) 2554.
[11] J. Zygmunt, F. Krumeich, R. Nesper, Adv. Mater. 15 (2003) 1538.
[12] F. Krumeich, H.J. Muhr, M. Niederberger, F. Bieri, B. Schnyder, R. Nesper, J. Am. Chem. Soc. 121 (1999) 8324.
[13] T. Ghoshal, S. Kar, S. Chaudhuri, Cryst. Growth Des. 7 (2007) 136.
[14] Y.S. Luo, S.Q. Li, Q.F. Ren, J.P. Liu, L.L. Xing, Y. Wang, Y. Yu, Z.J. Jia, J.L. Li, Cryst. Growth Des. 7 (2007) 87.
[15] W.Q. Zhang, L.Q. Xu, K.B. Tang, F.Q. Li, Y.T. Qian, Eur. J. Inorg. Chem. (2005) 653.
[16] M.H. Cao, T.F. Liu, S. Gao, G.B. Sun, X.L. Wu, C.W. Hu, Z.L. Wang, Angew. Chem. Int. Ed. 44 (2005) 4197.
[17] Y.S. Fu, X.W. Du, J. Sun, Y.F. Song, J. Liu, J. Phys. Chem. C 111 (2007) 3863.
[18] J.C. Boyer, F. Vetrone, L.A. Cuccia, J.A. Capobianco, J. Am. Chem. Soc. 128 (2006) 7444.
[19] Y.P. Fang, A.W. Xu, R.Q. Song, H.X. Zhang, L.P. You, J.C. Yu, H.Q. Liu, J. Am. Chem. Soc. 125 (2003) 16025.
[20] K. Riwotzki, H. Meyssamy, A. Kornowski, M. Haase, Angew. Chem. Int. Ed. 40 (2001) 573.
[21] S. Nishihama, T. Hirai, I. Komasawa, J. Mater. Chem. 12 (2002) 1053.
[22] K. Riwotzki, H. Meyssamy, A. Kornowski, M. Haase, J. Phys. Chem. B 104 (2000) 2824.
[23] P. Schuetz, F. Caruso, Chem. Mater. 14 (2002) 4509.
[24] S. Heer, O. Lehmann, M. Haase, H.U. Güdel, Angew. Chem. 115 (2003) 3288.
[25] H. Meyssamy, K. Riwotzki, A. Kornowski, S. Naused, M. Haase, Adv. Mater. 11 (1999) 840.
[26] Y.W. Zhang, Z.G. Yan, L.P. You, R. Si, C.H. Yan, Eur. J. Inorg. Chem. (2003) 4099.
[27] R. Kijkowska, E. Cholewka, B. Duszak, J. Mater. Sci. 38 (2003) 223.
[28] H. Onoda, H. Nariai, H. Naki, I. Motooka, Mater. Chem. Phys. 73 (2002) 19.
[29] X. Wang, X. Sun, D. Yu, B. Zou, Y. Li, Adv. Mater. 15 (2003) 1442.
[30] S. Heer, O. Lehmann, M. Haase, H.U. Güdel, Angew. Chem. Int. Ed. 42 (2003) 3179.
[31] Y. Kang, E.J. Kim, D.Y. Lee, H.D. Park, J. Alloys Compd. 347 (2002) 266.
[32] I.W. Lenggoro, B. Xia, H. Mizushima, K. Okuyama, N. Kijima, Mater. Lett. 50 (2001) 92.
[33] Y.P. Fang, A.W. Xu, W.F. Dong, Small 1 (2005) 967.
[34] K.S. Suslick, Ultrasound: It's Chemical, Physical and Biological Effects, VCH, Weinheim, Germany, 1988.
[35] J. Nanda, S. Sapra, D.D. Sarma, Chem. Mater. 12 (2000) 1018.
[36] A. Gedanken, Ultrason. Sonochem. 11 (2004) 47.
[37] M. Huang, S. Mao, H. Feick, H. Yan, Y. Wu, H. Kind, E. Weber, R. Russo, P. Yang, Science 292 (2001) 1897.
[38] A.W. Xu, Y.P. Fang, L.P. You, H.Q. Lin, J. Am. Chem. Soc. 125 (2003) 1494.
[39] X. Ma, H. Zhang, Y. Ji, J. Xu, D. Yang, Mater. Lett. 58 (2004) 1180.
[40] W.B. Bu, L.X. Zhang, Z.L. Hua, H.R. Chen, J.L. Shi, Cryst. Growth. Des. 7 (2007) 2305.
[41] R.X. Yan, X.M. Sun, X. Wang, Q. Peng, Y.D. Li, Chem. Eur. J. 11 (2005) 2183.
[42] M. Yu, J. Lin, S.B. Wang, Appl. Phys. A. 80 (2005) 353.
[43] P.Y. Jia, J. Lin, X.M. Han, M. Yu, Thin Solid Films 483 (2005) 122.
[44] C.C. Tang, Y. Bando, D. Golberg, R.Z. Ma, Angew. Chem. Int. Ed. 44 (2005) 576.
[45] M. Yu, J. Lin, J. Fu, H.J. Zhang, Y.C. Han, J. Mater. Chem. 13 (2003) 1413.
[46] K. Kömpe, H. Borchert, J. Storz, A. Lobo, S. Adam, T. Möller, H. Markus, Angew. Chem. Int. Ed. 42 (2003) 5513.
[47] G. Blasse, B.C. Grabmaier, Luminescent Materials, Springer, Berlin, 1994.
[48] A.J. Wojtowicz, M. Balcerzyk, E. Berman, A. Lempicki, Phys. Rev. B 49 (1994) 14880.